Manuscript

Rapid age assessment of glacial landforms in the Pyrenees using Schmidt Hammer exposure dating (SHED)

Matt D. Tomkins[1], Jason M. Dortch[1, 2], Philip D. Hughes[1], Jonny J. Huck[1], Andrew Stimson[1], Magali Delmas[3], Marc Calvet[3], and Raimon Pallàs[4]

[1]*Cryosphere Research at Manchester, Department of Geography, University of Manchester, Manchester, M13 9PL, United Kingdom*

[2]*Kentucky Geological Survey, 228 Mining and Mineral Resources Building, University of Kentucky, Lexington, KY 40506, United States of America*

[3]*UMR CNRS 7194 HNHP, Université de Perpignan Via Domitia, Perpignan, France*

[4]*Departament de Dinàmica de la Terra i de l'Oceà, Universitat de Barcelona, 08028 Barcelona, Spain*

ABSTRACT

Schmidt Hammer (SH) sampling of 54 ^{10}Be dated granite surfaces from the Pyrenees reveals a clear relationship between exposure and weathering through time (n = 52, $R^2 = 0.96$, $p < 0.01$) and permits the use of the SH as a numerical dating tool. To test this ^{10}Be-SH calibration curve, 100 surfaces were sampled from 5 ice-front positions in the Têt catchment, Eastern Pyrenees, with results verified against independent ^{10}Be and ^{14}C ages. Gaussian modelling differentiates Holocene (9.4 ± 0.6 ka), Younger Dryas (12.6 ± 0.9 ka), Oldest Dryas (16.1 ± 0.5 ka), Last Glacial Maximum (LGM: 24.8 ± 0.9 ka) and Würmian Maximum Ice Extent stages (MIE: 40.9 ± 1.1 ka). These data confirm comparable glacier lengths during the LGM and MIE (~300 m difference), in contrast to evidence from the Western Pyrenees (≥15 km), reflecting the relative influence of Atlantic and Mediterranean climates. Moreover, Pyrenean glaciers advanced significantly during the LGM, with a local maximum at ~25 ka, driven by growth of the Laurentide Ice Sheet, southward advection of the polar front and a solar radiation minimum in the Northern Hemisphere. This calibration curve is available at http://shed.earth to enable wider application of this method throughout the Pyrenees.

INTRODUCTION

The Quaternary glacial record of the Pyrenees is essential for reconstructing regional paleoclimate and provides crucial information on the response of terrestrial ice masses to variability in the North Atlantic atmosphere-ocean circulation system (Pallàs et al., 2010). However, determining causal links between climate and glacier response is predicated on the development of robust chronological frameworks. Recent advances in terrestrial cosmogenic nuclide (TCN) and optically stimulated luminescence (OSL) dating techniques and their application to glacial and glacio-fluvial deposits have helped constrain the chronology of Late Pleistocene glaciation (Würmian Stage) and in particular, the timing of the Würmian Maximum Ice Extent (MIE). ^{10}Be ages from Ariège (Delmas et al., 2011; 2015) and Malniu (Pallàs et al., 2010) show that MIE glaciers in the Eastern Pyrenees terminated just down-valley of Last Glacial Maximum limits (LGM; 23.3 - 27.5 ka; Hughes and Gibbard, 2015). This appears to contrast with glaciers in the Western Pyrenees, where LGM glaciers failed to reach MIE limits by ~15 km (Jalut et al., 1992; Calvet et al., 2011; Delmas, 2015), perhaps reflecting the contrasting influence of Atlantic and Mediterranean climates (Delmas et al., 2011). However, this hypothesis is limited by the relative scarcity of geochronological data and the increasing fragmentation of trunk glaciers into isolated ice masses during retreat and downwastage of the Pyrenean icefield. These difficulties, exacerbated by the fragmentary nature of the geomorphological record, preclude straightforward stratigraphic correlation of glacial deposits and have thus far prevented a Pyrenean-scale synthesis of post-Marine Isotope Stage (MIS) 4 glaciation.

TCN dating is well suited to address this knowledge gap as glacial deposits are well preserved in the Pyrenees. However, moraine stabilisation (Hallet and Putkonen, 1994) and nuclide inheritance (Putkonen and Swanson, 2003) can result in '*young*' and '*old*' ages respectively (Heyman et al., 2011; Murari et al., 2014). The most significant barrier to isolating these ages is the cost of TCN dating, which often precludes high-sample studies and in turn, prevents statistically robust identification and rejection of erroneous results. Thus, new cost and time-efficient dating techniques are necessary which complement existing radiometric techniques and can be applied widely to undated glacial landforms. In the British Isles, a clear relationship between TCN exposure ages and Schmidt Hammer (SH) rebound values (R-values) was recorded for 54 dated granite surfaces ($R^2 = 0.94$, $p < 0.01$; 0.8 - 23.8 ka; Tomkins et al., 2016, 2018) and permits the estimation of exposure time based on surface R-values. This TCN-SH calibration curve has been applied to glacial landforms in the Mourne Mountains (Barr et al., 2017) and the Lake District (Tomkins et al., 2016), with results consistent with existing radiometric ages (^{10}Be, ^{14}C). However, direct application of this calibration curve to Pyrenean deposits is unsuitable as long-term weathering rates exhibit systematic variability between climatic regimes (Riebe et al., 2004). This variability is likely significant between the temperate-oceanic climate of the British Isles and the comparatively dry, continental Pyrenees. In this paper, we develop and verify the first Pyrenean Schmidt Hammer exposure dating (SHED) calibration curve and generate new chronological data to constrain the deglacial chronology of the Têt glacier, a major outlet of the Pyrenean icefield. These new chronological data are supported by independent ^{10}Be ages, are consistent with previous geomorphological assessments (Delmas et al., 2008), and contribute significantly to our understanding of post-MIS 4 glacier dynamics.

METHODS

54 TCN dated granite surfaces were sampled using the N-Type Schmidt Hammer from across the Pyrenees (Fig. 1; Table. 1; Pallàs et al., 2006, 2010; Crest et al., 2017). Sampled surfaces (Fig. 2) include moraine boulders (n = 39) and ice-sculpted bedrock (n = 15) from a range of elevations (981 - 2817 m) and geomorphological settings. All surfaces were of sufficient size (Sumner and Nel, 2002) and were free of surface discontinuities (Williams and Robinson, 1983) and lichen (Matthews and Owen, 2008). Sampled surfaces were coarse to medium grained granite and granodiorite from the Hercynian Axial Zone (Crest et al., 2017). Axial Zone granites were uplifted during and after the late Cretaceous following collision of Europe and the Iberian microplate, with deformation ceasing at ~20-25 Ma, followed by post-orogenic uplift over the last ~10 Ma (Gunnell et al., 2009; Ortuño et al., 2013). The predominant style of weathering is sub-aerial, as evidenced by granular disintegration of the crystalline rock surface (André, 2002). There is no clear variability in grain size or rock composition between sites (Fig. 1B). 30 R-values were recorded per surface. This exceeds the recommendation of Niedzielski et al. (2009) of 20 R-values for granite surfaces (Min. sample size in terms of mean at $\alpha = 0.05$). Carborundum treatment was used to remove surface irregularities prior to testing (Katz et al., 2000; Cerna & Engel, 2011; Engel et al., 2011; Viles et al., 2011; Kłapyta, 2013). There is ongoing debate as to whether rock surfaces should be smoothed prior to testing (Moses et al., 2014). However, the data presented in this study indicates that a consistent sampling approach enables age-related information to be retained i.e. recently exposed surfaces (< 5 ka) generate significantly different R-values from those exposed during the Younger Dryas, the LGM and the Würmian MIE. R-values were recorded perpendicular to the tested surface to reduce the risk of

frictional sliding of the plunger tip (Viles et al., 2011), with single impacts separated by at least a plunger width (Aydin, 2009) and no outliers were removed following Niedzielski et al. (2009). Reported R-values are the arithmetic mean of 30 R-values and the standard error of the mean (SEM). To account for Schmidt Hammer drift with use (Tomkins et al., 2018), instrument calibration was based on the University of Manchester calibration boulder (Dortch et al., 2016) and performed using SHED-Earth, an online calculator developed to enable wider and more consistent application of SHED (Pre-data collection: 48.27 ± 2.02; Post-data collection: 48.23 ± 1.92; Correction Factor: 0.999).

^{10}Be exposure ages were recalibrated using the online calculators formerly known as the CRONUS-Earth online calculators (http://hess.ess.washington.edu/math/, Wrapper script 2.3, Main calculator 2.1, constants 2.3, muons 1.1; Balco et al., 2008). Exposure ages are based on the primary calibration dataset of Borchers et al. (2016), the time-dependent Lm scaling (Lal, 1991; Stone, 2000) and assuming 0 mm ka^{-1} erosion. This approach is suitable as erosion rates for most glaciated crystalline rock surfaces are usually low (0.1 – 0.3 mm ka^{-1}; André, 2002). Recalibrated ages must be treated as 'minimum' ages due to the potential impact of surface erosion or transient shielding by snow or sediment cover. Two ^{10}Be ages are likely compromised by prior exposure (*inheritance*) and are excluded from further analysis. Sample CAC28 from the Cometa d'Espagne cirque (26.96 ± 2.89 ka; Crest et al., 2017) is proximal (~2 m) to 3 tightly clustered bedrock ages (CAC25 = 10.85 ± 2.04 ka; CAC26 = 11.97 ± 1.86 ka; CAC27 = 11.95 ± 2.92 ka; Mean squared weighted deviation (MSWD) = 0.094). Similarly, sample ICM04 from the Malniu catchment (Age = 80.73 ± 7.92 ka; Pallàs et al., 2010) is proximal (~10 m) to 3 dated moraine boulders (ICM01 = 51.12 ± 4.84 ka; ICM02 = 43.91 ± 4.28 ka; ICM03 = 42.59 ± 4.15 ka; MSWD = 0.945). Both of these datasets are internally consistent (MSWD < 1; ICM01-03; CAC25-27), which suggests that prior exposure, rather than post-depositional exhumation, accounts for the positively skewed distribution of ^{10}Be ages. Remaining data (n = 52) are used to construct an ordinary least squares (OLS) regression from which numerical ages can be interpolated based on SH R-values.

To test for regional variation in rates of sub-aerial weathering, age control data (n = 52) were separated into sub-regions (Fig. 3A; Southern n = 46; Eastern n = 34; Central n = 18). These datasets were used to construct logarithmic regressions for each sub-region. For each sub-region regression, ages were calculated at R-value intervals of 0.1 over the associated calibration period (Southern = 4.1 - 51.1 ka; Eastern = 10.9 - 51.1 ka; Central = 4.1 - 18.2 ka). Interpolated ages were compared to the ages generated by the full age control dataset, with two-sample Students t-tests used to evaluate whether the difference between sub-region and full dataset results was statistically significant. Sub-region information is presented in Table 2.

To verify the suitability of this TCN-SH calibration curve, 100 granite surfaces were sampled from 5 ice-front positions along a ~18 km transect of the Têt catchment, Eastern Pyrenees (Fig. 4), with results validated against independent ^{10}Be and ^{14}C ages (Delmas et al., 2008) i.e. ^{10}Be ages that do not comprise one of the 52 age control surfaces that underpin the calibration curve (Fig. 1). Of the 26 ^{10}Be ages reported by Delmas et al. (2008), many post-date the timing of final deglaciation, likely due to moraine stabilisation processes (Hallet and Putknonen, 1994). Despite this limitation, these data, in additional to geomorphological mapping of moraine stages (Fig. 5), provide a useful chronological framework for ice recession in the Têt catchment and can be used as independent evidence to verify the results of SHED. Sampled sites include proximal inner (Site A, 1 km from catchment headwall, ~2200 m) and outer cirque moraines (Site B, 1.3 km, ~2168 m). Based on existing ^{10}Be ages, these moraines may reflect ice margin oscillations during the Younger Dryas or early-Holocene although considerable age scatter (n = 5; 12.00 - 13.99 ka) prevents accurate separation of glacial stages. Down-valley from these sites, glacially-deposited boulders adjacent to a prominent lateral moraine (Site C, 5.5 km, ~2051 m) are indicative of a post-LGM re-advance of the Têt glacier. This site is down-valley of the Grave-amont core site, which has produced ^{14}C ages in the range 19.47 - 20.26 ka cal BP (n = 3). These data suggest that the Têt glacier was confined to the cirque environment as early as ~20 ka. Further south, a large terminal moraine (Site D, 18.5 km, ~1686 m), dated to 24.22 ± 4.58 ka (n = 1), likely marks the LGM ice extent. ^{10}Be ages from this glacial stage exhibit considerable scatter (n = 6; 15.6 - 24.2 ka) and likely reflect post-depositional exhumation of moraine boulders (Hallet and Putkonen, 1994). As a result, the precise age of this landform is unclear, which limits our understanding of the dynamics of the Têt glacier during the global LGM. Finally, ~300 m outside of the LGM limit, the two outermost moraines of the Têt glacier (Site E, 18.8 km, ~1624 m) mark the Würmian MIE, although the precise age of this landform is unclear. These moraines record the maximum extent of glaciation in the Têt catchment, as the downstream landscape is dominated by fluvial incision. These moraines are morphologically distinct from proximal LGM moraines (Delmas et al. 2008) but it is not currently clear whether these landforms were deposited synchronously, with the outer moraines subject to intense moraine stabilisation processes since the LGM, or instead, whether the outer moraines represent an earlier glacial stage (MIS 3-4; Calvet et al., 2011). At each site, 20 surfaces were sampled for SHED following the methods described above, with SH exposure ages and 1σ uncertainties calculated using SHED-Earth (http://shed.earth; Tomkins et al., 2018). To account for geological uncertainty which typically displays as positive and negative skew of datasets, probability density estimates (PDEs) were produced and modelled to separate out the highest probability Gaussian distribution (Fig. 5) as per the methods of Dortch et al. (2013). Using the KS density kernel in MATLAB (2015) and a dynamic smoothing window based on age uncertainty, PDE peaks and tails were separated into individual Gaussian distributions, the sum of which integrates to the cumulative PDE at 1000 iterations to obtain the best fit. The re-integrated PDE (made from the isolated Gaussians) goodness of fit is indicated graphically (Dortch et al., 2013). Full sample information for the 100 surfaces sampled in the Têt catchment can be found in the Supplementary Dataset.

RESULTS

A clear correlation between TCN exposure ages and SH R-values is expressed by a logarithmic regression (Fig. 1A; n = 52, $R^2 = 0.96$, $p = < 0.01$). Boulder height (Fig. 3B; n = 38; $R^2 = < 0.01$; $p = 0.97$), sample elevation (Fig. 3C; $R^2 = 0.11$; $p = 0.02$) and cirque headwall distance (Fig. 3D; $R^2 = 0.09$; $p = 0.04$) have a negligible correlation with R-values. Significant differences in R-values between recently exposed surfaces (< 5 ka; R-values > 60) and those exposed during the Younger Dryas (R-values ~50), the LGM (R-values ~40) and the Würmian MIE (R-values ≤ 30) indicates that age-related information can be retained with carborundum treatment (Moses et al., 2014). There is no significant variation in sub-aerial weathering rate between sub-regions (Table 2; Fig. 3A) as *eastern* (n = 34), *central* (n = 18) and *southern* curves (n = 46) are completely enclosed by the 1σ boundaries of the full dataset curve and generate SH ages that vary from the full dataset by ≤ 0.37 ka, ≤ 0.93 ka and ≤ 0.22 ka respectively. In addition, the average sub-region variation from the full dataset is limited to 0.11 ± 0.06 ka and 0.14 ± 0.08 ka for the *southern* and *eastern* datasets respectively, increasing to 0.43 ± 0.22 ka for the *central* dataset. This likely reflects the limited calibration period (4.1 - 18.2 ka) and low number of age control surfaces (n = 18) for the *central* dataset. As a result, TCN-SH calibration curves should be based on large age control datasets (≥ 25 ^{10}Be ages; Tomkins et al., 2016; 2018) to minimise the effect of individual exposure age errors. Despite this, two-sample Students t-tests indicate that variation between age estimates derived from the full dataset and *southern*, *eastern* and *central* datasets is not statistically significant (Table 2; p values >0.91).

In the Têt catchment, Schmidt Hammer sampling of undated glacially-deposited boulders reveals statistically significant differences (Two-sample Students t-tests, p < 0.01) between the mean SH R-values of sequential glacial landforms (A-B, B-C, C-D, D-E). Statistically significant differences in mean SH R-values are evident between both proximal (~300 m; A-B; D-E) and distal landforms (~13 km; C-D). These data were converted into numerical ages based on the TCN-SH calibration curve presented in this paper ($y = 44.02\ln(x) + 186.55$) although these must be considered minimum ages as post-depostional erosion is assumed to be negligible (0 mm ka^{-1}). Incorporating an erosion rate of 0.3 mm ka^{-1} (André, 2002) increases calibration ^{10}Be ages (n = 52) by ≤ 1.43% and by an average of ~0.64%, equivalent to ~0.7 ka for sample ICM01 (~50 ka) and ≤ 0.16 ka for surfaces exposed within the last ~25 ka. This variation is within measurement uncertainty for ^{10}Be ages and is significantly less than the 1σ uncertainty of individual SH exposure ages (Min. = 1.69 ka; Max. = 1.85 ka). As a result, incorporating erosion has a negligible impact on calculated SH exposure ages, even for landforms deposited prior to the LGM. To account for geological uncertainty in interpolated ages, PDE modelling (Dortch et al., 2013) produces peak Gaussian distributions for glacial landforms in the Têt catchment of (A) 9.41 ± 0.62 ka, (B) 12.62 ± 0.91 ka, (C) 16.08 ± 0.46 ka, (D) 24.80 ± 0.90 ka and (E) 40.86 ± 1.09 ka.

DISCUSSION

Firstly, a strong correlation between ^{10}Be ages and SH R-values indicates that the primary control on surface R-values is cumulative exposure to sub-aerial weathering (Tomkins et al., 2016; 2018). This correlation is observed despite marked variability in sample elevations (Elevation range = ~1836 m), boulder heights (Height = ~0.5 to ~3.5 m), cirque headwall distances (~0.6 to ~22 km) and relative positions along the axis of the Pyrenean mountain range (Fig. 1B; Max. distance between samples = ~110 km). These data match previous evidence from the British Isles (Tomkins et al., 2016; 2018) and the Krkonoše Mountains, Poland/Czech Republic (Engel, 2007; Engel et al., 2011) for a relationship between ^{10}Be ages and sub-aerial weathering of granite surfaces. However, clear differences in effective calibration timescales in the British Isles (~25 ka), the Krkonoše Mountains (~15 ka) and the Pyrenees (~50 ka) indicates that weathering rates vary significantly between these regions, likely as a function of latitudinal gradients in either precipitation or temperature. The data presented in this study also provide further evidence that weathering rates are not linear but decrease over time (White and Brantley, 2003; Stahl et al., 2013). For surfaces exposed prior to the LGM, slower rates of weathering likely reflect the formation of stable weathering residues which slow water transport to unaltered material and impede chemical transport away from it (Colman, 1981). Finally, these data imply little variation in the rate of rock surface weathering between sub-regions over the last ~50 ka (Table 2; Fig. 3A). It must be noted that this interpretation is based on the assumption that recalibrated ^{10}Be ages are accurate ages for deglaciation, with no post-depositional erosion. If this assumption is not valid, then variable regional weathering rates could influence ^{10}Be ages and introduce bias to the SHED calibration curve as distal surfaces exposed synchronously could return contrasting ^{10}Be ages. However, under the assumption of minimal weathering of crystalline rock surfaces (0-3 mm ka^{-1}; André, 2002), post-depositional erosion is unlikely to have significant impact on the results of SHED as differences in ^{10}Be ages due to erosion are significantly smaller than ^{10}Be measurement uncertainty (Sample ICM01; ^{10}Be age uncertainty = ± 4.99 ka; Age difference 0-3 mm ka^{-1} erosion = ~0.7 ka). This appears to constrast with recent evidence from New Zealand, with marked local variability in rates of rock surface weathering (Stahl et al., 2013). This variability necessitates local calibration curves for proximal sites (~100 km distance) which are applicable over contrasting calibration timescales (Saxton and Charwell River terraces = ~10 ka; Waipara River terraces = ~1 ka; c.f. Fig. 2 in Stahl et al., 2013). New data from the Pyrenees indicate that sub-aerial weathering of granite surfaces is consistent across the Central and Eastern Pyrenees which implies that equivalent time-dependent weathering of granite surfaces can occur over significant spatial scales for regions of similar climate (Tomkins et al., 2016; 2018).

In the Têt catchment, age estimates derived from PDE modelling of Gaussian distributions (Dortch et al., 2013) are in correct stratigraphic order, are consistent with existing interpretations of post-MIE glaciation (Fig. 5) and are supported by independent ^{10}Be ages which provide a chronological framework for the retreat dynamics of the Têt glacier during the Würmian (Delmas et al., 2008). Gaussian ages clearly differentiate LGM (D; 24.80 ± 0.90 ka) and Würmian MIE (E; 40.86 ± 1.09 ka) glacial deposits and provide firm evidence of comparable glacier lengths during MIS 2 and MIS 3 (~300 m difference). This contrasts markedly with evidence from the Western Pyrenees, where glaciers failed to reach MIE limits during the LGM (≥15 km difference; Gállego catchment; Jalut et al., 1992; Calvet et al., 2011). The proximity of MIE and LGM deposits matches the geomorphological record in Malniu (~330 m) and Querol (~600m) and indicates that glaciers in the Eastern Pyrenees advanced significantly during MIS 2 to near MIE limits, irrespective of glacier size (Querol: ~25 km, Têt: ~18.5 km, Malniu: ~6 km). A MIS 3 Würmian MIE (40.86 ± 1.09 ka) matches ages from a terminal moraine in Malniu (TCN; n = 3; 42.6 – 51.1 ka; Pallàs et al., 2010), a mid-valley lateral moraine in the Ariege (TCN; n = 1; 37.89 ± 9.98 ka; Delmas et al., 2011) and OSL ages from the Senegüe terminal moraine in the Gállego catchment (n = 2; ~36 ka; Lewis et al., 2009). These data contrast with MIS 4 ages from ice-contact lake deposits in the Cinca catchment (OSL; n = 3; 46 – 71 ka; Lewis et al., 2009) and from the terminal moraine in the Ariege catchment (TCN; n = 1; 88.78 ± 18.37 ka; Delmas et al., 2011). Regardless of the precise timing of the MIE, one of the most valuable contributions of SHED is its ability to differentiate proximal LGM and MIE glacial deposits and thus, enable robust comparison of glacier length fluctuations across the Pyrenees.

By comparison, the timing of the local MIS 2 glacial maximum in the Têt catchment is constrained by both TCN (n = 1; 24.22 ± 4.58 ka) and SHED ages (n = 13; 24.80 ± 0.90 ka). These data accord with recent evidence that ice masses in the European Alps reached their maximum extents at 24-26 ka due to the growth of the Laurentide Ice Sheet, which reached its maximum close to this time (>23.0 ± 0.6 ka; Ullman et al., 2015), and the southward advection of the polar front (Monegato et al., 2017). These events coincided with reduced solar radiation towards the solar minimum in the northern hemisphere at ~24 ka (Alley et al., 2002). In addition to SHED and TCN ages from the Têt catchment, an Alpine LGM is supported by post-maximum TCN ages from Querol (YRA Samples; n = 3; 22.7 – 24.2 ka), the oldest ages from the frontal lobe (OEC01; 23.8 ± 2.3 ka) and a coeval lateral moraine (LAF04; 25.7 ± 2.7 ka) in Malniu (Pallàs et al., 2010), and ^{14}C ages from the Gállego catchment, which indicate that the MIS 2 MIE occurred by 24.21 ka cal. BP (Jalut et al., 1992). The asynchroneity of Alpine glaciers and the Eurasian ice sheets at the global LGM, the latter reaching its maximum extent at ~21 ka (Hughes et al., 2016), demonstrates the sensitivity of Alpine ice masses to the advection of moisture from the Mediterranean Sea (Luetscher et al., 2015). The contrasting size of Pyrenean glaciers at the LGM likely reflects the relative influence of weather systems from the Atlantic and the western Mediterranean, the latter favouring cyclogenesis, convection of moist air and increased precipitation to coastal mountain ranges (Kuhlemann et al., 2008). However, this hypothesis is tentative owing to limited geochronological data for MIS 2 glaciers in the Western Pyrenees. SHED is a viable method to address this knowledge gap as the calibration curve is well constrained by age control points which span the global LGM and is able to reproduce the LGM TCN age in the Têt catchment, varying by <0.6 ka.

Finally, the geomorphological record indicates that post-LGM retreat was dynamic (Fig. 5; Borde and Cirque Stages). A number of re-advance events are captured by SHED, with moraines deposited during the Oldest Dryas (C: 16.08 ± 0.46 ka), Younger Dryas (B: 12.62 ± 0.91 ka) and early-Holocene (A: 9.41 ± 0.62 ka). Evidence for a significant re-advance during the Oldest Dryas is matched by TCN ages from the Orri (CPM; n = 3; 16.41 ± 0.58 ka) and Malniu catchments (IMA; n = 5; 16.68 ± 0.52 ka) and is consistent with evidence for major advances in the Western Pyrenees (Palacios et al., 2017). However, these data conflict markedly with ^{14}C ages from the Grave-amont core site (Fig. 5; 19.47 - 20.26 ka cal BP) which indicate rapid post-LGM retreat (~3.3 km ka^{-1}). New SHED data indicates that this deposit must have been overridden (Delmas et al., 2008; Crest et al., 2017). In addition, SHED clearly differentiates proximal (~300 m) Younger Dryas (YD; B, 12.62 ± 0.91 ka) and Holocene moraines (A, 9.41 ± 0.62 ka). TCN exposure ages from the YD moraine (Sample N; 12.0 ± 2.2 ka) and proximal bedrock surfaces (Sample O2; 13.4 ± 2.1 ka) give contrasting age estimates but are broadly consistent with the SHED estimate. The age of the inner cirque moraine (A) overlaps with the 9.3 ka event (Rasmussen et al., 2014) although complete deglaciation and re-advance of ice in the Têt catchment after the YD seems unlikely owing to the short-timeframe of this cooling event (~110 yr). Instead, this moraine likely marks a standstill or re-advance of the ice margin from sheltered cirques below Pic Cometa d'Espagne. These data in their totality indicate that cirque (A-B) and valley moraines (C) reflect still-stands or re-advances of the Têt glacier, potentially in response to North Atlantic climate fluctuations (OD, YD, 9.3 ka event). These glacial deposits provide a valuable record of ice margin fluctuations and yet the post-LGM history of the Pyrenean icefield is currently poorly understood (Calvet et al., 2011). Future research using SHED must seek to accurately differentiate post-LGM ice masses to provide robust information on the response of these glaciers to North Atlantic climate variability.

This new SHED calibration curve demonstrates that this method can be applied successfully in contrasting climatic regimes and that equivalent time-dependent weathering of granite surfaces can occur within regions of similar climate (Tomkins et al., 2016; 2018). TCN-SH calibration curves based on significant age-controls datasets (n ≥ 50) have been shown to produce robust ages for glacial landforms, as demonstrated through comparison with independent radiometric ages (^{10}Be), and in aggregate, can generate results of comparable accuracy and precision to TCN dating. This approach could be replicated in similar well-dated granite regions throughout the world (e.g. Himalaya, Patagonia, Sierra Nevada) and has the ability to revolutionise high-sample low-budget quantitative studies in Quaternary Science. In the Pyrenees, future applications of SHED are needed to (1) separate LGM and Würmian MIE landforms across the mountain range and to (2) address gaps in our understanding of post-LGM retreat (Calvet et al., 2011). The relative scarcity of geochronological data, particularly in the Western Pyrenees, has thus far prevented a Pyrenean-scale synthesis of post-MIS 4 glaciation, although progress continues to be made (e.g. Palacios et al., 2017). Widespread application of SHED across the Pyrenees would generate a wealth of new chronological data related to glacier oscillations over the last ~50 ka and would likely accelerate progress in our understanding of the last Pleistocene glacial cycle.

To apply this regional calibration curve to undated landforms or to verify its accuracy on landforms dated using radiometric methods (TNC, OSL, ^{14}C), users should follow the methods described above and perform (1) instrument calibration and (2) age calibration procedures as described fully in Tomkins et al. (2018). To perform instrument calibration, users should sample a suitable surface before and after data collection which returns R-values which lie within the range of R-values measured in the field (Tomkins et al., 2018). In contrast, instrument calibration using the test anvil (R-value = 81 ± 2; Proceq, 2004) is inappropriate for surfaces typically tested by Quaternary researchers (R-values: 25 - 60) and should only be utilised for the hardest natural rock surfaces (R-values ≥ 70). To perform age calibration and to standardise different Schmidt Hammers and different user strategies to the Pyrenean calibration curve, users should test their Schmidt Hammer on one of three calibration surfaces provided (Mean of 30 R-values; Table 3; Sample photos available at http://shed.earth) rather than the University of Manchester calibration boulder as described in Dortch et al. (2016). Users should compare the recorded mean R-value against the assigned value (Table 3) to calculate a correction factor which is then all applied to user data. This functionality is incorporated into SHED-Earth. These procedures facilitate comparison between studies and encourage wider and more consistent application of SHED throughout the Pyrenees.

CONCLUSIONS

Quaternary deposits in the Pyrenees are ideally placed for paleoclimate studies given their proximity to both the North Atlantic and the Mediterranean. However, limited geochronological datasets, the increasing fragmentation of trunk glaciers, and the incomplete nature of the geomorphological record, have prevented a regional scale synthesis of post-MIS 4 glaciation. The Pyrenees are ideally suited for Schmidt Hammer exposure dating (SHED) given the excellent preservation of glacial deposits and the abundance of granite glacial boulders and erosion surfaces.

In this study, we show that SHED is a viable geochronological technique, as a strong correlation between 52 TCN exposure ages and SH R-values ($R^2 = 0.96$, $p < 0.01$) permits the use of the SH as a numerical dating tool. The effectiveness of this method is demonstrated for the Têt catchment in the Eastern Pyrenees, where SH exposure ages are in correct stratigraphic order, are consistent with existing geomorphological interpretations, and show excellent agreement with previous TCN ages. SHED data confirm comparable glacier lengths during the LGM and the MIE in the Eastern Pyrenees (~300 m), in contrast to evidence from the Western Pyrenees (>15 km), and also confirm the antiquity of the MIE which likely occurred during MIS 3 (40.86 ± 1.09 ka). Moreover, SHED data show that glaciers in the Eastern Pyrenees reached their maximum extents during the global LGM, synchronous with Alpine ice masses (24 - 26 ka). Glacier expansion was driven by enhanced moisture availability caused by southward advection of the polar front coinciding with the maximum extent of the Laurentide Ice Sheet and a solar minimum at ~24 ka.

SHED is cost and time-efficient and can differentiate proximal glacial deposits (~300 m) and in aggregate, can generate results of comparable accuracy and precision to TCN dating. Moreover, our approach provides new evidence for non-linear weathering of granitic surfaces through time, likely associated with the formation of stable weathering residues. Finally, our data imply little variation in the rate of sub-aerial weathering between sub-regions over the last ~50 ka, which indicates that our calibration curve can be applied widely throughout the Central and Eastern Pyrenees.

ACKNOWLEDGMENTS

This project was supported by the Royal Geographical Society (with IBG) with a Dudley Stamp Memorial Award and by the University of Manchester SEED Fieldwork Support Fund. Dortch, Hughes and Huck would like to thank the University of Manchester Research Stimulation Fund. We would also like to thank Prof. John Matthews, associate editor Prof. James Shulmeister and an anonymous reviewer for their constructive reviews.

REFERENCES

Alley, R. B., Brook, E. J., & Anandakrishnan, S. (2002). A northern lead in the orbital band: north–south phasing of Ice-Age events. *Quaternary Science Reviews*, *21*(1), 431-441. https://doi.org/10.1016/S0277-3791(01)00072-5

André, M. F. (2002). Rates of postglacial rock weathering on glacially scoured outcrops (Abisko-Riksgränsen Area, 68°N). *Geografiska Annaler, Series A: Physical Geography*, *84*, 139–150. https://doi.org/10.1111/j.0435-3676.2002.00168.x

Balco, G., Stone, J. O., Lifton, N. A., & Dunai, T. J. (2008). A complete and easily accessible means of calculating surface exposure ages or erosion rates from ^{10}Be and ^{26}Al measurements. *Quaternary Geochronology*, *3*, 174–195. https://doi.org/10.1016/j.quageo.2007.12.001

Barr, I. D., Roberson, S., Flood, R., & Dortch, J. (2017). Younger Dryas glaciers and climate in the Mourne Mountains, Northern Ireland. *Journal of Quaternary Science*, *32*(1), 104–115. https://doi.org/10.1002/jqs.2927

Borchers, B., Marrero, S., Balco, G., Caffee, M., Goehring, B., Lifton, N.,Nishiizumi, K., Phillips, F., Schaefer, J., & Stone, J. (2016). Geological calibration of spallation production rates in the CRONUS- Earth project. *Quaternary Geochronology*, *31*, 188–198. https://doi.org/10.1016/j.quageo.2015.01.009

Calvet, M., Delmas, M., Gunnell, Y., & Bourle, D. (2011). Recent Advances in Research on Quaternary Glaciations in the Pyrenees. In J. Ehlers, P. L. Gibbard, & P. D. Hughes (Eds.), *Quaternary Glaciations, Extent and Chronoloy, a closer look Part IV* (Vol. 15, pp. 127–139). Elsevier. https://doi.org/10.1016/B978-0-444-53447-7.00011-8

Cĕrná, B., & Engel, Z. (2011). Surface and sub-surface Schmidt hammer rebound value variation for a granite outcrop. *Earth Surface Processes and Landforms*, *36*, 170-179. https://doi.org/10.1002/esp.2029

Colman, S. M. (1981). Rock-Weathering Rates as Functions of Time. *Quaternary Research*, *264*(15), 250–264. https://doi.org/10.1016/0033-5894(81)90029-6

Crest, Y., Delmas, M., Braucher, R., Gunnell, Y., Calvet, M., & ASTER Team. (2017). Cirques have growth spurts during deglacial and interglacial periods: Evidence from ^{10}Be and ^{26}Al nuclide inventories in the central and eastern Pyrenees. *Geomorphology*, *278*, 60–77. https://doi.org/10.1016/j.geomorph.2016.10.035

Delmas, M, (2015). The last maximum ice extent and subsequent deglaciation of the Pyrenees: an overview of recent research. *Cuadernos de Investigación Geográfica*, *41*, 109-137. http://dx.doi.org/10.18172/cig.2708

Delmas, M., Gunnell, Y., Braucher, R., Calvet, M., & Bourlès, D. (2008). Exposure age chronology of the last glaciation in the eastern Pyrenees. *Quaternary Research*, *69*, 231–241. https://doi.org/10.1016/j.yqres.2007.11.004

Delmas, M., Calvet, M., Gunnell, Y., Braucher, R., & Bourlès, D. (2011). Palaeogeography and ^{10}Be exposure-age chronology of Middle and Late Pleistocene glacier systems in the northern Pyrenees: Implications for reconstructing regional palaeoclimates. *Palaeogeography,* *Palaeoclimatology, Palaeoecology*, *305*(1–4), 109–122. https://doi.org/10.1016/j.palaeo.2011.02.025

Delmas, M., Braucher, R., Gunnell, Y., Guillou, V., Calvet, M., & Bourlès, D. (2015). Constraints on Pleistocene glaciofluvial terrace age and related soil chronosequence features from vertical ^{10}Be profiles in the Ariège River catchment (Pyrenees, France). *Global and Planetary Change*, *132*, 39-53. https://doi.org/10.1016/j.gloplacha.2015.06.011

Dortch, J. M., Owen, L. A., & Caffee, M. W. (2013). Timing and climatic drivers for glaciation across semi-arid western Himalayan-Tibetan orogen. *Quaternary Science Reviews*, *78*, 188–208. https://doi.org/10.1016/j.quascirev.2013.07.025

Dortch, J. M., Hughes, P.D., & Tomkins, M. D. (2016) Schmidt hammer exposure dating (SHED): Calibration boulder of Tomkins et al. (2016). *Quaternary Geochronology*, *35*, 67-68. https://doi.org/10.1016/j.quageo.2016.06.001

Engel, Z. (2007). Measurement and age assignment of intact rock strength in the Krkonoše Mountains, Czech Republic. *Zeitschrift für Geomorphologie*, *51*, 69-80. https://doi.org/10.1127/0372-8854/2007/0051S-0069

Engel, Z., Traczyk, A., Braucher, R., Woronko, B., & Křížek, M. (2011). Use of ^{10}Be exposure ages and Schmidt hammer data for correlation of moraines in the Krkonoše Mountains, Poland/Czech Republic. *Zeitschrift für Geomorphologie*, *55*(2), 175-196. https://doi.org/10.1127/0372-8854/2011/0055-0036

Gunnell, Y., Calvet, M., Brichau, S., Carter, A., Aguilar, J.-P., & Zeyen, H. (2009). Low long-term erosion rates in high-energy mountain belts: insights from thermo- and biochronology in the Eastern Pyrenees. *Earth and Planetary Science Letters*, *278*, 208-218. https://doi.org/10.1016/j.epsl.2008.12.004

Hallet, B., & Putkonen, J. (1994). Surface Dating of Dynamic Landforms: Young Boulders on Aging Moraines. *Science*, *265*(5174), 937–940. http://doi.org/10.1126/science.265.5174.937

Heyman , J., Stroeven, A. P., Harbor, J. M., & Caffee, M. W. (2011). Too young or too old: Evaluating cosmogenic exposure dating based on analysis of compiled boulder exposure ages. *Earth and Planetary Science Letters*, *302*(1-2), 71-80. https://doi.org/10.1016/j.epsl.2010.11.040

Hughes, P. D., & Gibbard, P. L. (2015). A stratigraphical basis for the Last Glacial Maximum (LGM). *Quaternary International*, *383*, 174-185. https://doi.org/10.1016/j.quaint.2014.06.006

Hughes, A. L., Gyllencreutz, R., Lohne, Ø. S., Mangerud, J., & Svendsen, J. I. (2016). The last Eurasian ice sheets–a chronological database and time-slice reconstruction, DATED-1. *Boreas*, *45*(1), 1-45. https://doi.org/10.1111/bor.12142

Jalut, G., Monserrat Marti, J., Fontugne, M., Delibrias, G., Vilaplana, J. M., & Julia, R. (1992). Glacial to interglacial vegetation changes in the northern and southern Pyrenees: deglaciation, vegetation cover and chronology. *Quaternary Science Reviews*, *11*, 449–480. https://doi.org/10.1016/0277-3791(92)90027-6

Katz, O., Reches, Z., & Roegiers, J.-C. (2000). Evaluation of mechanical rock properties using the Schmidt Hammer. *International Journal of Rock Mechanics and Mining Sciences*, *37*, 723-728. https://doi.org/10.1016/S1365-1609(00)00004-6

Kłapyta, P. (2013). Application of Schmidt hammer relative age dating to Late Pleistocene moraines and rock glaciers in the Western Tatra Mountains, Slovakia. *Catena*, *111*, 104-121. http://dx.doi.org/10.1016/j.catena.2013.07.004

Kuhlemann, J., Rohling, E. J., Krumrei, I., Kubik, P., Ivy-Ochs, S., & Kucera, M. (2008). Regional synthesis of Mediterranean atmospheric circulation during the Last Glacial Maximum. *Science*, *321*(5894), 1338-1340. https://doi.org/10.1126/science.1157638

Lal, D. (1991). Cosmic ray labeling of erosion surfaces: in situ nuclide production rates and erosion models. *Earth and Planetary Science Letters*, *104*, 424–439. https://doi.org/10.1016/0012-821X(91)90220-C

Lewis, C. J., Mcdonald, E. V, Sancho, C., Peña, J. L., & Rhodes, E. J. (2009). Climatic implications of correlated Upper Pleistocene glacial and fluvial deposits on the Cinca and Gállego Rivers (NE Spain) based on OSL dating and soil stratigraphy. *Global and Planetary Change*, *67*(3–4), 141–152. https://doi.org/10.1016/j.gloplacha.2009.01.001

Luetscher, M., Boch, R., Sodemann, H., Spötl, C., Cheng, H., Edwards, R. L., Frisia, S., Hof, F., & Müller, W. (2015). North Atlantic storm track changes during the Last Glacial Maximum recorded by Alpine speleothems. *Nature Communications*, *6*. https://doi.org/10.1038/ncomms7344

Matthews, J. A., & Owen, G. (2008). Endolithic lichens, rapid biological weathering and schmidt hammer r-values on recently exposed rock surfaces: Storbreen glacier foreland, jotunheimen, Norway. *Geografiska Annaler, Series A: Physical Geography*, *90*(4), 287–297. https://doi.org/10.1111/j.1468-0459.2008.00346.x

Monegato, G., Scardia, G., Hajdas, I., Rizzini, F., & Piccin, A. (2017). The Alpine LGM in the boreal ice- sheets game. *Scientific Reports*, 7(2078), 1–8. https://doi.org/10.1038/s41598-017-02148-7

Moses, C., Robinson, D., and Barlow, J. (2014). Methods for measuring rock surface weathering and erosion. *Earth-Science Reviews*, *135*, 141-161. http://dx.doi.org/10.1016/j.earscirev.2014.04.006

Murari, M.K., Owen, L.A., Dortch, J.M., Caffee, M.W., Dietsch, C., Fuchs, M., Haneberg, W.C., Sharma, M.C., & Townsend-Small, A. (2014). Timing and climatic drivers for glaciation across monsoon-influenced regions of the Himalayan-Tibetan orogen. *Quaternary Science Reviews*, *88*, 159-182. https://doi.org/10.1016/j.quascirev.2014.01.013

Niedzielski, T., Migoń, P., & Placek, A. (2009). A minimum sample size required from Schmidt hammer measurements. *Earth Surface Processes and Landforms*, *34*, 1713–1725. https://doi.org/10.1002/esp

Ortuño, M., Martí, A., Martín-Closas, C., Jiménez-Moreno, G., Martinetto, E., & Santanach, P. (2013). Palaeoenvironments of the Late Miocene Prüedo Basin: implications for the uplift of the Central

Pyrenees. *Journal of the Geological Society*, *170*, 79–92. https://doi.org/10.1144/jgs2011-121

Palacios, D., García-Ruiz, J. M., Andrés, N., Schimmelpfennig, I., Campos, N., Léanni, L., & ASTER Team. (2017). Deglaciation in the central Pyrenees during the Pleistocene–Holocene transition: Timing and geomorphological significance. *Quaternary Science Reviews*, *162*, 111-127. https://doi.org/10.1016/j.quascirev.2017.03.007

Pallàs, R., Rodés, Á., Braucher, R., Bourlès, D., Delmas, M., Calvet, M., & Gunnell, Y. (2010). Small, isolated glacial catchments as priority targets for cosmogenic surface exposure dating of Pleistocene climate fluctuations, southeastern Pyrenees. *Geology*, (10), 891–894. https://doi.org/10.1130/G31164.1

Pallàs, R., Rodés, Á., Braucher, R., Carcaillet, J., Ortuño, M., Bordonau, J., Bourlès. D., Vilaplana, J. M., Masana, E., & Santanach, P. (2006). Late Pleistocene and Holocene glaciation in the Pyrenees: a critical review and new evidence from ^{10}Be exposure ages, south-central Pyrenees. *Quaternary Science Reviews*, *25*, 2937–2963. https://doi.org/10.1016/j.quascirev.2006.04.004

Proceq. (2004). Operating Instructions Betonprüfhammer N/NR- L/LR. Schwerzenbach.

Putkonen, J., & Swanson, T. (2003). Accuracy of cosmogenic ages for moraines. *Quaternary Research*, *59*, 255–261. https://doi.org/10.1016/S0033-5894(03)00006-1

Rasmussen, S. O., Bigler, M., Blockley, S. P., Blunier, T., Buchardt, S. L., Clausen, H. B., Cvijanovic, I., Dahl-Jensen, D., Johnsen, S. J., Fischer, H., Gkinis, V., Guillevic, M., Hoek, W. Z., Lowe, J. J., Pedro, J. B., Popp, T., Seierstad, I. K., Steffensen, J. P., Svensson, A. M., Vallelonga, P., Vinther, B. M., Walker, M. J. C., Wheatley, J. J., & Winstrup, M. (2014). A stratigraphic framework for abrupt climatic changes during the Last Glacial period based on three synchronized Greenland ice-core records: refining and extending the INTIMATE event stratigraphy. *Quaternary Science Reviews*, *106*, 14–28. https://doi.org/10.1016/j.quascirev.2014.09.007

Riebe, C. S., Kirchner, J. W., & Finkel, R. C. (2004). Erosional and climatic effects on long-term chemical weathering rates in granitic landscapes spanning diverse climate regimes. *Earth and*

Planetary Science Letters, *224*, 547–562. https://doi.org/10.1016/j.epsl.2004.05.019

Stahl, T., Winkler, S., Quigley, M., Bebbington, M., Duffy, B., & Duke, D. (2013). Schmidt hammer exposure-age dating (SHD) of late quaternary fluvial terraces in New Zealand. *Earth Surface Processes and Landforms*, *38*(15), 1838-1850. https://doi.org/10.1002/esp.3427

Stone, J. O. (2000). Air pressure and cosmogenic isotope production. *Journal of Geophysical Research*, *105*(1), 23753–23759. https://doi.org/10.1029/2000JB900181

Sumner, P., & Nel, W. (2002). The effect of rock moisture on Schmidt hammer rebound: Tests on rock samples from Marion Island and South Africa. *Earth Surface Processes and Landforms*, *27*(10), 1137–1142. https://doi.org/10.1002/esp.402

Tomkins, M. D., Dortch, J. M., & Hughes, P. D. (2016). Schmidt Hammer exposure dating (SHED): Establishment and implications for the retreat of the last British Ice Sheet. *Quaternary Geochronology*, *33*, 46–60. https://doi.org/10.1016/j.quageo.2016.02.002

Tomkins, M. D., Huck, J.J., Dortch, J. M., Hughes, P. D., Kirkbride, M., & Barr, I. (2018). Schmidt Hammer exposure dating (SHED): Calibration procedures, new exposure age data and an online calculator. *Quaternary Geochronology*, 44, 55-62. https://doi.org/10.1016/j.quageo.2017.12.003

Ullman, D. J., Carlson, A. E., LeGrande, A. N., Anslow, F. S., Moore, A. K., Caffee, M., Syverson, K. M., & Licciardi, J. M. (2015). Southern Laurentide ice-sheet retreat synchronous with rising boreal summer insolation. *Geology*, *43*(1), 23-26. https://doi.org/10.1130/G36179.1

Viles, H., Goudie, A., Grab, S., & Lalley, J. (2011). The use of the Schmidt Hammer and Equotip for rock hardness assessment in geomorphology and heritage science: A comparative analysis. *Earth Surface Processes and Landforms*, *36*(3), 320–333. https://doi.org/10.1002/esp.2040

White, A. F., & Brantley, S. L. (2003). The effect of time on the weathering of silicate minerals: why do weathering rates differ in the laboratory and field? *Chemical Geology*, *202*, 479–506.

https://doi.org/10.1016/j.chemgeo.2003.03.001

Williams, R. B. G., & Robinson, D. A. (1983). The effect of surface texture on the determination of the surface hardness of rock using the schmidt hammer. Earth Surface Processes and Landforms, 8(3), 289–292. https://doi.org/10.1002/esp.3290080311

Figure Captions

Figure 1. Schmidt Hammer exposure dating (SHED) calibration curve for the Pyrenees. A: Correlation between Schmidt Hammer R-values and terrestrial cosmogenic nuclide (TCN) exposure ages (n = 53). Inherited outlier ICM04 not shown as it is beyond the graph axis (Age = 80.7 ± 7.9 ka, R-value = 24.98 ± 1.17). B: Map of age control sites, sites referred to in text (A: Ariege, C: Campcardós, Ci: Cinca G: Gállego, T: Têt) and the Last Glacial Maximum extent after Calvet et al. (2011).

Figure 2. ^{10}Be dated surfaces sampled using the Schmidt Hammer. A: Holocene, B: Younger Dryas, C: Last Glacial Maximum (LGM) and D: Würmian Maximum Ice Extent (MIE) dated surfaces from Pallas et al. (2010) and Crest et al. (2017). Reported ^{10}Be ages were recalibrated using the online calculators formerly known as the CRONUS-Earth online calculators (Balco et al., 2008). Reported R-values are the arithmetic mean of 30 R-values (excluding no outliers) ± the Standard Error of the Mean (SEM).

Figure 3. Local and regional controls on surface R-values. A: Full dataset (*black*) and sub-region calibration curves for the southern (*blue*), eastern (*red*) and central Pyrenees (*green*). Sub-region calibration curves fall within 1σ (dark grey) and 2 σ (light grey) prediction limits of the full dataset curve and imply no significant variation in the rate of rock surface weathering between sub-regions. B: Boulder height (m) and surface R-values (n = 38). C: Sample elevation (m) and surface R-values (n = 52). D: Cirque headwall distance (km) and surface R-values (n = 52). These data (A-D) imply that site specific factors have a negligible impact on sub-aerial weathering of granite surfaces in the

Central and Eastern Pyrenees.

Figure 4. Sampled sites for Schmidt Hammer exposure dating (SHED) from the Têt catchment, Eastern Pyrenees. A: Holocene (Site A; 9.41 ± 0.62 ka) and Younger Dryas moraines (Site B; 12.62 ± 0.91 ka). B: The prominent lateral moraine and proximal surfaces sampled for SHED (Site C: 16.08 ± 0.46 ka). C: Sampled surface from the large terminal moraine, previously dated to 24.22 ± 4.58 ka (^{10}Be; n = 1; Delmas et al., 2008), which marks the maximum extent of ice during the Last Glacial Maximum (Site D: 24.80 ± 0.90 ka). D: The outermost moraine of the Têt glacier and the Würmian Maximum Ice Extent for this catchment (Site E: 40.86 ± 1.09 ka).

Figure 5. A deglacial chronology for the Têt catchment, Eastern Pyrenees. A: Geomorphological map showing the Würmian Maximum Ice Extent (MIE) for the Têt, Angoustrine and Formiguères glaciers. Moraine stages modified and TCN exposure ages recalibrated from Delmas et al. (2008). Schmidt Hammer sampled sites (A-E) are shown. B: Probability density estimates (PDEs) and Gaussian models for sampled sites (A-E) are plotted against the NGRIP δ^{18}O curve (Rasmussen et al., 2014). Key events are shown: Younger Dryas (YD), Oldest Dryas (OD), Global Last Glacial Maximum (GLGM), Local Last Glacial Maximum (LLGM) and the Eurasian Last Glacial Maximum (ELGM).

Table Captions

Table 1. Details of ^{10}Be dated surfaces sampled using the Schmidt Hammer.

Table 2. Analysis of sub-region datasets and comparison with the full age control dataset (n = 52). These data imply little variation in the rate of sub-aerial weathering between sub-regions.

Table 3. Age calibration surfaces for the Pyrenees. Detailed information on age calibration can be found in Tomkins et al. (2018) or at http://shed.earth. Users should test their Schmidt Hammer on one of these calibration surfaces provided (Mean of 30 R-values) and input their results into the SHED-Earth online calculator. Age calibration standardises different Schmidt Hammers and user strategies to the regional calibration curve.

Figure 1

Click here to download Figure Tomkins_Fig1_900dpi.png

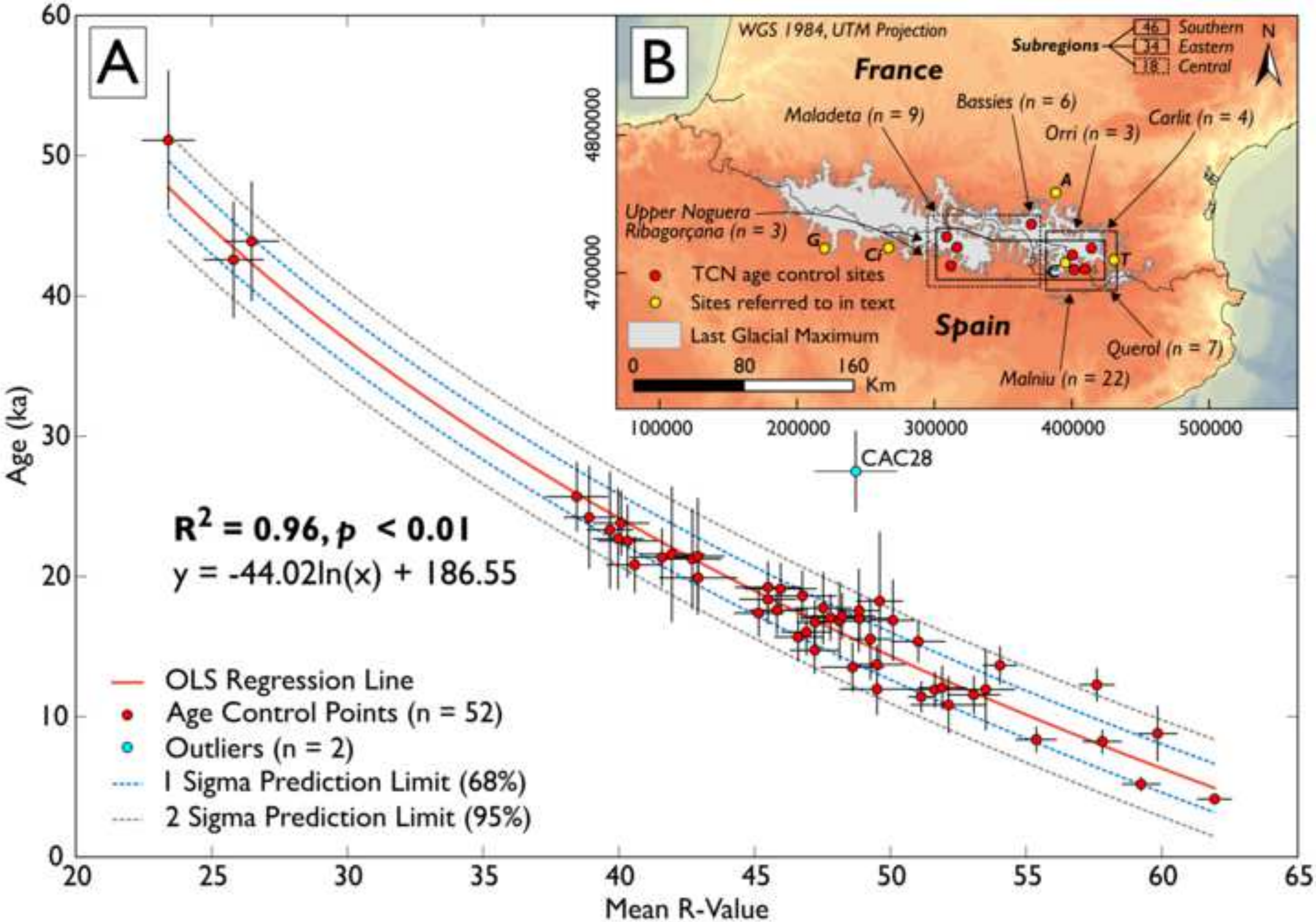

Figure 2

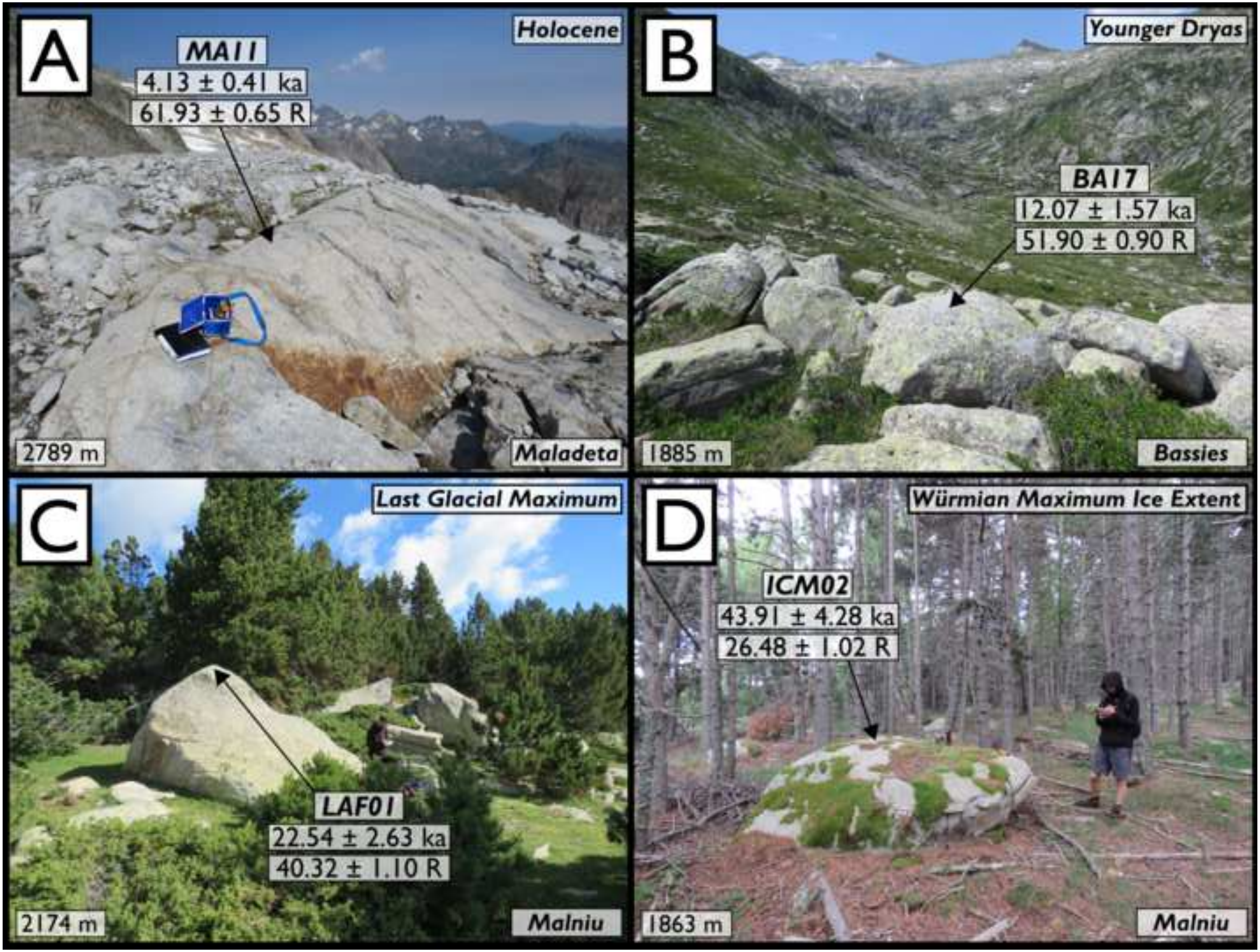
A
Holocene
MA11
4.13 ± 0.41 ka
61.93 ± 0.65 R
2789 m
Maladeta
B
Younger Dryas
BA17
12.07 ± 1.57 ka
51.90 ± 0.90 R
1885 m
Bassies
C
Last Glacial Maximum
LAF01
22.54 ± 2.63 ka
40.32 ± 1.10 R
2174 m
Malniu
D
Würmian Maximum Ice Extent
ICM02
43.91 ± 4.28 ka
26.48 ± 1.02 R
1863 m
Malniu

Figure 3

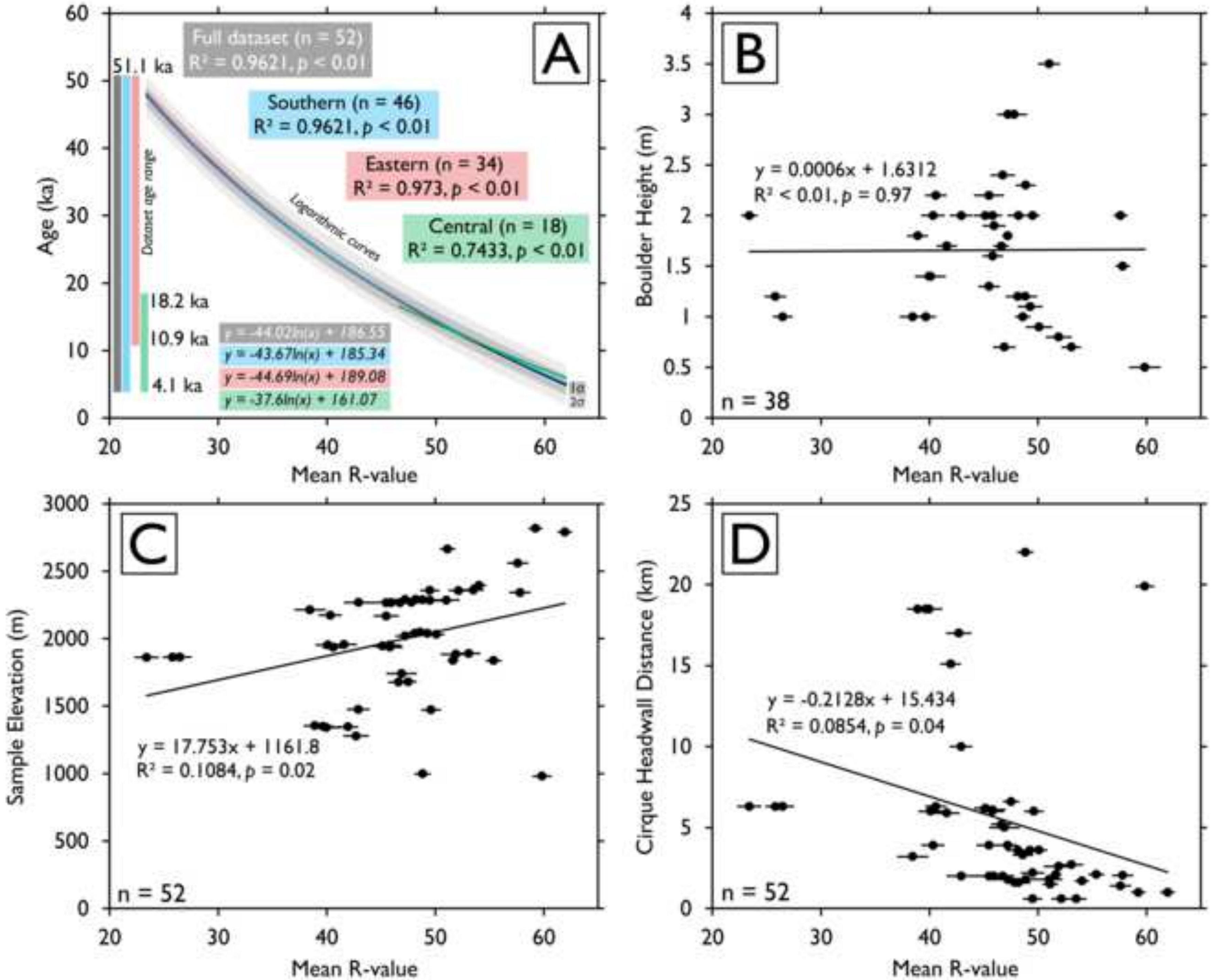
A
Full dataset (n = 52)
R² = 0.9621, p < 0.01
Southern (n = 46)
R² = 0.9621, p < 0.01
Eastern (n = 34)
R² = 0.973, p < 0.01
Central (n = 18)
R² = 0.7433, p < 0.01
51.1 ka
Dataset age range
Logarithmic curves
18.2 ka
10.9 ka
4.1 ka
y = -44.02ln(x) + 186.55
y = -43.67ln(x) + 185.34
y = -44.69ln(x) + 189.08
y = -37.6ln(x) + 161.07
1σ
2σ
Age (ka)
Mean R-value
B
y = 0.0006x + 1.6312
R² < 0.01, p = 0.97
n = 38
Boulder Height (m)
Mean R-value
C
y = 17.753x + 1161.8
R² = 0.1084, p = 0.02
n = 52
Sample Elevation (m)
Mean R-value
D
y = -0.2128x + 15.434
R² = 0.0854, p = 0.04
n = 52
Cirque Headwall Distance (km)
Mean R-value

Figure 4 Click here to download Figure Tomkins_Fig4_600dpi.png

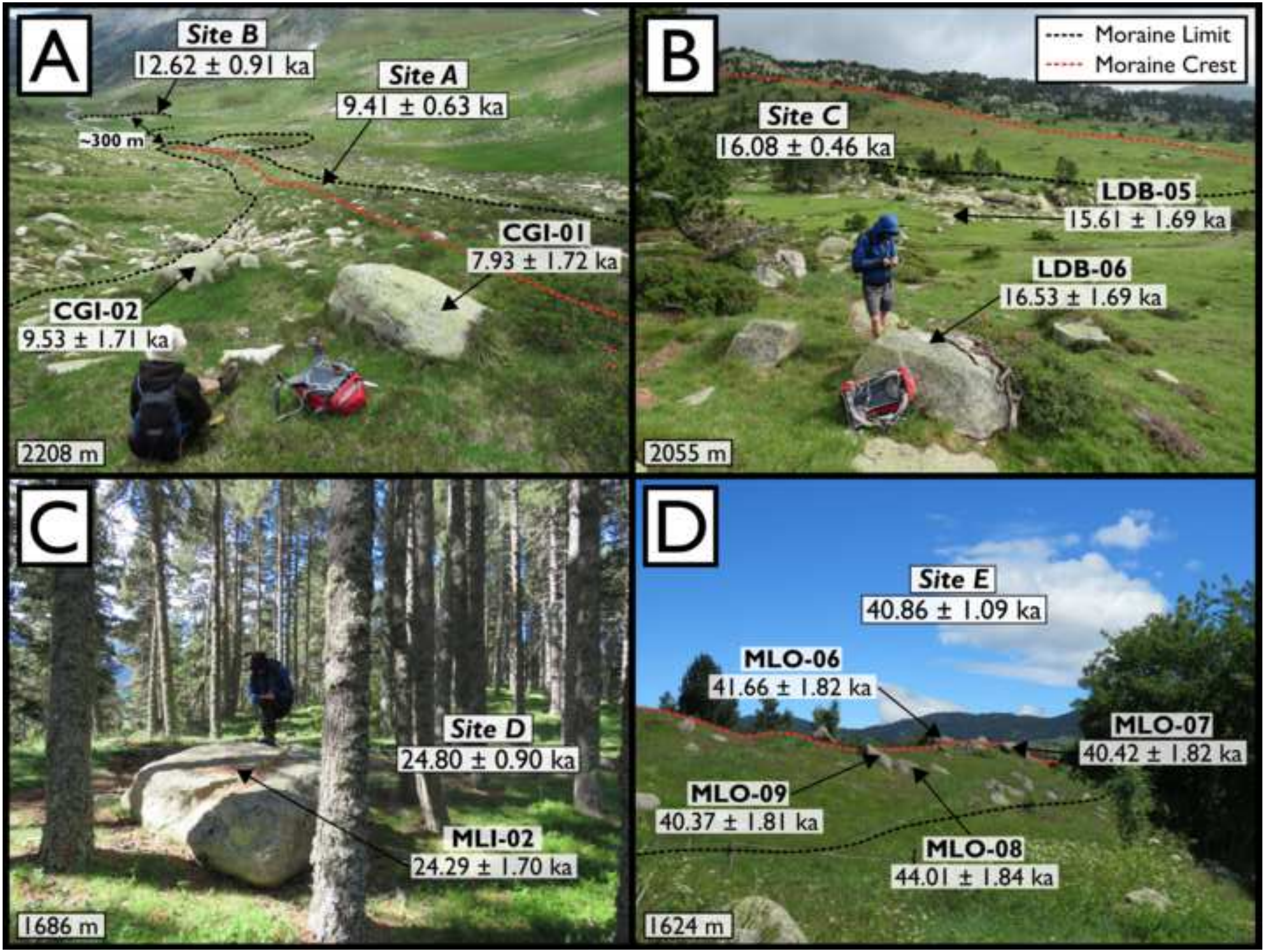

Figure 5

Click here to download Figure Tomkins_Fig5_900dpi.png

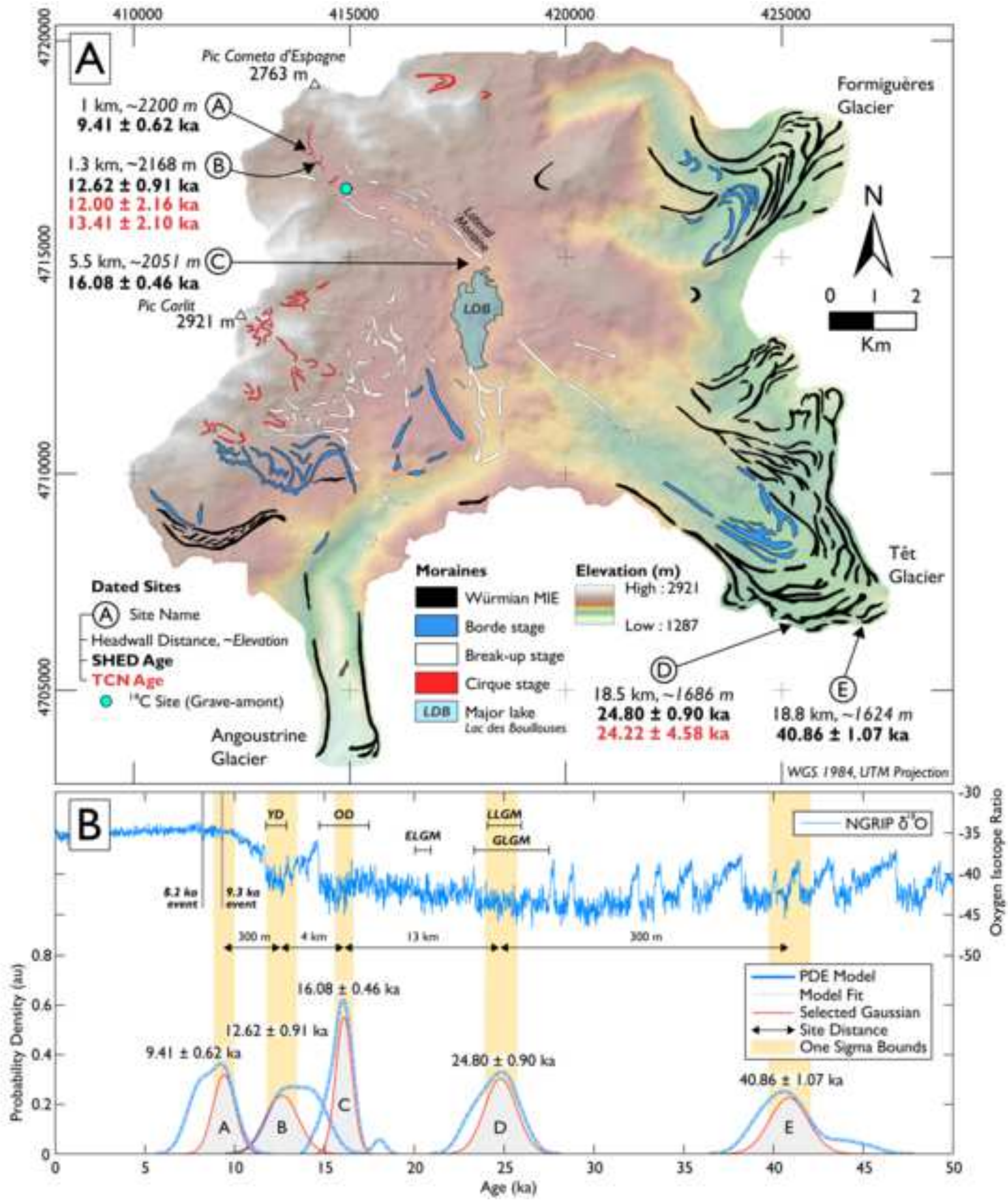

Table 1

Sample	Coordinates [a]		Elevation (m)	Type	Sub-region [b]	Boulder height (m)	Cirque distance (km)	Mean R-Value	SEM [c]	Age (ka)	1σ
MA03	306645	4726398	2396	Bedrock	S + C	-	1.7	54.03	0.65	13.67	1.36
MA04	306659	4725978	2560	Boulder	S + C	2	1.4	57.60	0.67	12.29	1.21
MA11	306498	4725387	2789	Bedrock	S + C	-	1	61.93	0.65	4.13	0.41
MA12	306627	4725290	2817	Bedrock	S + C	-	1	59.23	0.71	5.21	0.52
MA07	306901	4725631	2665	Bedrock	S + C	-	1.5	51.13	0.49	11.43	1.12
MA05	306959	4726408	2342	Boulder	S + C	1.5	2.05	57.80	0.73	8.24	0.88
MA06	306991	4726657	2283	Boulder	S + C	2	2.2	49.50	1.04	13.73	1.41
AN02	308872	4726401	2050	Boulder	S + C	1	3.3	48.60	1.18	13.54	1.77
AN01	308669	4726819	2020	Boulder	S + C	1.8	3.9	47.20	0.91	14.74	1.69
STA01	311923	4704290	998	Boulder	S + C	1.2	22	48.84	0.82	17.58	2.98
SMV01	312411	4706093	981	Boulder	S + C	0.5	19.9	59.84	0.74	8.80	1.99
RHL01	316483	4718607	1472	Bedrock	S + C	-	6	49.60	0.87	18.25	4.95
BA15	371797	4735829	1678	Boulder	C	1.7	5.2	46.60	0.89	15.69	1.74
BA16	371426	4736078	1741	Boulder	C	0.7	5	46.90	0.94	16.05	1.69
BA20	369354	4734473	1837	Bedrock	C	-	2.10	51.64	0.95	11.94	1.29
BA19	369354	4734473	1837	Bedrock	C	-	2.1	55.37	0.76	8.38	0.93
BA17	369697	4734705	1885	Boulder	C	0.8	2.6	51.90	0.90	12.07	1.57
BA18	369717	4734785	1890	Boulder	C	0.7	2.7	53.07	0.99	11.57	1.37
FUL03	403443	4707445	1476	Bedrock	S + E	-	10	42.90	0.99	21.45	4.17
LAT01	408106	4702521	1279	Bedrock	S + E	-	17	42.70	1.07	21.26	3.59
YRA-21	408727	4701033	1341	Boulder	S + E	1.4	18.5	39.97	0.94	22.69	3.62
YRA-20	408719	4701031	1349	Boulder	S + E	1	18.5	39.67	0.86	23.32	4.19
YRA-19	408651	4701040	1354	Boulder	S + E	1.8	18.5	38.90	0.94	24.22	3.67
CAC25	414113	4718126	2356	Bedrock	S + E	-	0.6	52.14	1.41	10.85	2.04
CAC26	414113	4718126	2357	Bedrock	S + E	-	0.6	49.51	1.38	11.97	1.85
CAC27	414113	4718126	2360	Bedrock	S + E	-	0.6	53.51	1.09	11.95	2.92
CAC28	414113	4718126	2356	Bedrock	-	-	0.6	48.71	1.53	26.93 [d]	2.89
QRS01	406616	4703876	1346	Bedrock	S + E	-	15.1	41.95	1.21	21.59	4.84
ICM01	404800	4702660	1861	Boulder	S + E	2	6.3	23.41	0.98	51.11	4.99
ICM02	404787	4702624	1863	Boulder	S + E	1	6.3	26.48	1.02	43.91	4.28
ICM03	404764	4702592	1863	Boulder	S + E	1.2	6.3	25.81	1.12	42.59	4.15
ICM04	404736	4702569	1864	Boulder	-	1.5	6.3	24.98	1.17	80.73 [d]	7.92
OEC5	404606	4702925	1935	Boulder	S + E	2.2	6.3	40.58	1.06	20.84	2.04
OEC4	404545	4702828	1945	Boulder	S + E	2	6.2	45.15	0.92	17.39	1.70
OEC6	404548	4703058	1937	Boulder	S + E	1.6	6.1	45.82	0.98	17.58	1.73
OEC3	404415	4702566	1951	Boulder	S + E	2	6	45.82	1.02	17.61	1.74
OEC2	404329	4702532	1956	Boulder	S + E	1.7	5.9	41.58	1.20	21.37	2.09
OEC1	404402	4702668	1953	Boulder	S + E	1.4	6	40.08	1.03	23.81	2.32
LAF03	402597	4701952	2168	Boulder	S + E	2.2	3.9	45.49	1.22	19.23	1.87
LAF01	402493	4701917	2174	Boulder	S + E	2	3.9	40.32	1.10	22.54	2.63
LAF04	401565	4701602	2213	Boulder	S + E	1	3.2	38.45	1.15	25.69	2.50
OMA04	400874	4702314	2267	Boulder	S + E	1.3	2	45.49	1.05	18.38	1.79
OMA02	400871	4702326	2268	Boulder	S + E	2	2	42.92	1.44	19.91	1.93
OMA03	400877	4702330	2267	Boulder	S + E	2.4	2	46.76	1.26	18.62	1.81
OMA01	400884	4702332	2267	Boulder	S + E	1.9	2	45.95	1.34	19.13	1.86
IMA03	400931	4703060	2287	Boulder	S + E	2.3	1.8	48.86	1.07	17.02	1.66
IMA01	400943	4703050	2289	Boulder	S + E	3	1.8	47.22	0.68	16.72	1.63
IMA02	400924	4703031	2286	Boulder	S + E	3.5	1.8	51.02	1.01	15.37	1.50
IMA04	401069	4703262	2270	Boulder	S + E	3	1.6	47.79	1.09	17.08	1.66
IMA05	401073	4703284	2290	Boulder	S + E	2	1.6	48.22	1.22	17.19	1.67
CPM03	400965	4712601	2032	Boulder	S + E	0.9	3.6	50.09	0.82	16.87	2.91
CPM01	400805	4712550	2039	Boulder	S + E	1.2	3.6	48.12	1.09	16.83	2.81
CPM02	400809	4712566	2038	Boulder	S + E	1.1	3.6	49.26	0.76	15.54	2.90
CAS03	403474	4710840	1681	Bedrock	S + E	-	6.6	47.52	1.05	17.75	2.59

[a] with reference to WGS 1984 31 T, [b] S = Southern, C = Central, E = Eastern, [c] Standard Error of the Mean, [d] Inherited surface

Table 2

Region	# ages	Age Range (ka)	R-Value Range[a]	Regression Equation	R^2	p value	Mean variation[b]	Mean uncertainty[c]	Max. variation	p value[d]	Interpretation[e]
Full Dataset	52	4.1 - 51.1	25 - 60	y = -44.02ln(x) + 186.55	0.9621	< 0.01	-	1.725 ± 0.031	-	-	-
Southern	46	4.1 - 51.1	25 - 60	y = -43.67ln(x) + 185.34	0.9621	< 0.01	0.11 ± 0.06 ka	1.725 ± 0.031	0.22 ka	0.91	H_0
Eastern	34	10.9 - 51.1	25 - 54	y = -44.69ln(x) + 189.08	0.973	< 0.01	0.14 ± 0.08 ka	1.728 ± 0.036	0.37 ka	0.92	H_0
Central	18	4.1 - 18.2	46 - 60	y = -37.6ln(x) + 161.07	0.7433	< 0.01	0.43 ± 0.22 ka	1.704 ± 0.008	0.90 ka	0.98	H_0

[a] Ages interpolated at R-value interval of 0.1 within these ranges, [b] Mean variation from Full Dataset ± Mean Absolute Deviation, [c] Mean calibration curve uncertainty of the Full Dataset ± Mean Absolute Deviation over the associated calibration period, [d] p value of two-sample Students t-tests assuming unequal variance, [e] H_1 - The difference between the two populations is statistically significant at $p = 0.05$, H_0 - The difference between the two populations is not statistically significant at $p = 0.05$

Table 3

Name	UTM Coordinates [a]		Elevation (m)	Mean R-Value	SEM[b]
Maladeta Calibration Boulder	307424	4727841	1906	52.60	0.74
Bassies Calibration Boulder	374343	4733594	853	44.14	0.60
Carlit Calibration Boulder	422066	4707335	1820	48.67	0.65

[a] with reference to WGS 1984 31 T, [b] Standard Error of the Mean

Site	Sample ID	Latitude (°)	Longitude (°)	Elevation (m)	Mean R-Value	MAD[a]	SEM[b]	Age (ka)	1σ
A	CGI-01	42.607017	1.952433	2238	57.84	3.53	0.80	7.93	1.72
	CGI-02	42.606861	1.95218	2235	55.77	4.51	1.05	9.53	1.71
	CGI-03	42.606823	1.951876	2226	57.14	5.73	1.28	8.47	1.71
	CGI-04	42.606635	1.952086	2223	58.81	3.83	0.85	7.20	1.72
	CGI-05	42.606501	1.9521	2214	56.48	4.64	1.01	8.98	1.71
	CGI-06	42.606437	1.95204	2213	57.78	4.03	0.93	7.98	1.72
	CGI-07	42.606062	1.952364	2207	57.74	3.22	0.74	8.01	1.72
	CGI-08	42.605765	1.952466	2208	56.01	4.07	0.90	9.35	1.71
	CGI-09	42.605515	1.952653	2195	55.51	5.00	1.18	9.74	1.71
	CGI-10	42.605363	1.952753	2193	57.88	4.96	1.13	7.90	1.72
	CGI-11	42.605147	1.952745	2186	55.78	5.15	1.21	9.53	1.71
	CGI-12	42.604889	1.953176	2188	55.58	6.50	1.37	9.69	1.71
	CGI-13	42.604872	1.953261	2183	57.38	4.70	1.06	8.29	1.71
	CGI-14	42.604664	1.953143	2184	56.01	4.00	0.90	9.35	1.71
	CGI-15	42.604396	1.953379	2174	54.71	7.03	1.47	10.38	1.71
	CGI-16	42.604096	1.953116	2173	58.41	3.60	0.86	7.50	1.72
	CGI-17	42.604168	1.953066	2168	55.88	5.89	1.32	9.45	1.71
	CGI-18	42.604328	1.952819	2187	57.21	4.73	1.00	8.41	1.71
	CGI-19	42.604096	1.952153	2183	56.45	5.87	1.26	9.01	1.71
	CGI-20	42.604096	1.95208	2184	56.38	4.63	1.04	9.06	1.71
B	CGO-01	42.602443	1.954558	2177	51.35	5.96	1.25	13.18	1.70
	CGO-02	42.602373	1.954717	2176	49.61	4.41	0.98	14.69	1.70
	CGO-03	42.602373	1.954717	2176	51.08	4.47	0.93	13.40	1.70
	CGO-04	42.602401	1.95479	2167	50.21	5.09	1.10	14.16	1.70
	CGO-05	42.602401	1.95479	2167	50.21	5.11	1.16	14.16	1.70
	CGO-06	42.602348	1.954937	2170	52.25	5.32	1.16	12.41	1.70
	CGO-07	42.602213	1.955013	2162	52.41	6.07	1.29	12.27	1.70
	CGO-08	42.602215	1.955208	2169	49.38	5.06	1.06	14.89	1.70
	CGO-09	42.602287	1.955194	2163	49.61	4.33	0.93	14.69	1.70
	CGO-10	42.602307	1.955389	2166	51.61	6.48	1.45	12.95	1.70
	CGO-11	42.602263	1.95556	2171	50.08	4.61	1.03	14.27	1.70
	CGO-12	42.602291	1.955645	2164	52.95	4.53	0.95	11.82	1.70
	CGO-13	42.602382	1.955766	2165	51.61	6.51	1.35	12.95	1.70
	CGO-14	42.602436	1.955728	2165	51.98	5.57	1.22	12.63	1.70
	CGO-15	42.602472	1.955691	2165	51.91	5.58	1.29	12.69	1.70
	CGO-16	42.602545	1.955799	2167	49.88	5.39	1.14	14.45	1.70
	CGO-17	42.602589	1.955701	2167	49.98	4.24	0.98	14.36	1.70
	CGO-18	42.602705	1.955553	2166	52.48	4.40	1.08	12.21	1.70
	CGO-19	42.602749	1.955442	2169	52.15	7.06	1.49	12.49	1.70
	CGO-20	42.602785	1.955442	2169	50.05	3.51	0.86	14.30	1.70
	LDB-01	42.582627	1.99748	2046	45.95	3.62	0.94	18.06	1.69
	LDB-02	42.582494	1.997653	2046	47.58	5.54	1.24	16.53	1.69
	LDB-03	42.582358	1.997582	2047	47.55	4.56	0.99	16.56	1.69
	LDB-04	42.582286	1.99751	2046	48.65	4.57	0.98	15.55	1.69

	LDB-05	42.582141	1.997464	2048	48.58	4.46	1.02	15.61	1.69
	LDB-06	42.582015	1.997466	2051	47.58	4.77	1.07	16.53	1.69
	LDB-07	42.581978	1.997381	2052	48.35	4.80	1.05	15.82	1.69
	LDB-08	42.581968	1.997198	2054	48.08	3.60	0.80	16.06	1.69
	LDB-09	42.58193	1.997028	2055	48.08	5.34	1.14	16.06	1.69
C	LDB-10	42.581829	1.996847	2056	48.18	4.32	0.98	15.97	1.69
	LDB-11	42.581853	1.996493	2059	48.42	4.04	0.91	15.76	1.69
	LDB-12	42.581869	1.996274	2058	49.08	4.53	1.03	15.16	1.69
	LDB-13	42.58174	1.995935	2058	47.98	4.63	1.02	16.16	1.69
	LDB-14	42.581766	1.995763	2058	47.72	3.95	0.86	16.40	1.69
	LDB-15	42.581746	1.995557	2052	48.38	5.02	1.13	15.79	1.69
	LDB-16	42.581773	1.995495	2050	49.05	4.50	0.97	15.19	1.69
	LDB-17	42.581736	1.995423	2051	48.02	5.40	1.23	16.12	1.69
	LDB-18	42.581762	1.995288	2048	48.02	5.87	1.21	16.12	1.69
	LDB-19	42.581644	1.995181	2048	49.89	4.93	1.08	14.44	1.70
	LDB-20	42.581687	1.995034	2048	49.35	4.62	1.05	14.92	1.70
	MLI01	42.509716	2.101574	1703	40.25	7.37	1.61	23.89	1.70
	MLI02	42.509871	2.101743	1699	39.89	4.34	0.99	24.29	1.70
	MLI03	42.509926	2.101936	1699	38.79	4.32	0.99	25.52	1.71
	MLI04	42.510077	2.102738	1699	40.69	4.07	0.92	23.42	1.70
	MLI05	42.509967	2.103713	1688	40.96	5.61	1.23	23.13	1.70
	MLI06	42.510328	2.103854	1687	40.02	5.34	1.21	24.14	1.70
	MLI07	42.51022	2.104963	1685	39.72	3.61	0.84	24.47	1.70
	MLI08	42.510503	2.10541	1683	39.82	4.51	1.05	24.36	1.70
	MLI09	42.510651	2.105894	1686	39.12	5.19	1.22	25.14	1.70
D	MLI10	42.510681	2.10632	1685	38.79	3.50	0.81	25.52	1.71
	MLI11	42.510836	2.106512	1683	39.36	5.54	1.23	24.88	1.70
	MLI12	42.510873	2.106695	1684	38.39	4.22	0.89	25.98	1.71
	MLI13	42.511027	2.106826	1684	38.15	4.74	1.05	26.25	1.71
	MLI14	42.511128	2.107032	1684	40.46	4.19	1.02	23.67	1.70
	MLI15	42.511346	2.107309	1684	41.06	5.77	1.30	23.02	1.70
	MLI16	42.511528	2.107489	1683	39.26	5.24	1.16	24.99	1.70
	MLI17	42.511747	2.107887	1680	41.32	5.57	1.17	22.73	1.70
	MLI18	42.512164	2.108246	1679	39.26	4.52	1.00	24.99	1.70
	MLI19	42.512435	2.10834	1679	39.36	4.36	1.02	24.88	1.70
	MLI20	42.512498	2.108339	1679	38.96	5.52	1.22	25.33	1.71
	MLO01	42.51083	2.111576	1619	27.38	6.26	1.43	40.85	1.81
	MLO02	42.510621	2.111348	1619	28.35	5.40	1.31	39.32	1.80
	MLO03	42.510485	2.111253	1618	27.48	5.77	1.23	40.69	1.81
	MLO04	42.510306	2.111316	1618	27.98	5.51	1.27	39.89	1.80
	MLO05	42.510251	2.111244	1618	24.78	5.45	1.22	45.24	1.86
	MLO06	42.510224	2.11122	1617	26.88	4.81	1.15	41.66	1.82
	MLO07	42.510215	2.111317	1618	27.65	6.03	1.43	40.42	1.81
	MLO08	42.510006	2.111052	1617	25.48	6.70	1.42	44.01	1.84
	MLO09	42.509898	2.110981	1618	27.68	6.18	1.35	40.37	1.81

E	MLO10	42.509887	2.110774	1619	27.55	5.30	1.19	40.58	1.81
	MLO11	42.509731	2.110338	1621	28.15	6.02	1.40	39.63	1.80
	MLO12	42.509657	2.110108	1622	26.82	8.22	1.81	41.77	1.82
	MLO13	42.509457	2.109916	1622	28.59	6.10	1.32	38.96	1.79
	MLO14	42.509383	2.109613	1623	26.82	4.86	1.11	41.77	1.82
	MLO15	42.509292	2.109578	1624	27.45	6.13	1.38	40.74	1.81
	MLO16	42.508837	2.108963	1632	28.49	5.03	1.11	39.11	1.79
	MLO17	42.508762	2.108514	1635	27.35	7.29	1.49	40.90	1.81
	MLO18	42.508762	2.108502	1636	28.49	5.90	1.31	39.11	1.79
	MLO19	42.50865	2.108089	1637	25.78	4.39	1.05	43.50	1.84
	MLO20	42.508586	2.107932	1637	27.02	5.07	1.13	41.44	1.82

[a] Mean Absolute Deviation, [b] Standard Error of the Mean